

## **Total absence of dystrophin expression exacerbates ectopic myofibre calcification, fibrosis and alters macrophage infiltration patterns.**

Christopher NJ Young<sup>1,2</sup>, Maxime RF Gosselin<sup>1</sup>, Robin Rumney<sup>1</sup>, Aleksandra Oksiejuk<sup>1,3</sup>, Natalia Chira<sup>1</sup>, Lukasz Bozycki<sup>4</sup>, Paweł Matryba<sup>5,6</sup>, Kacper Łukasiewicz<sup>7</sup>, Alex P Kao<sup>8</sup>, Joseph Dunlop<sup>9</sup>, Samuel C Robson<sup>1,10</sup>, Krzysztof Zabłocki<sup>4</sup> and Dariusz C Górecki<sup>1,11§</sup>

<sup>1</sup>Molecular Medicine, School of Pharmacy and Biomedical Sciences, University of Portsmouth, UK; <sup>2</sup>Leicester School of Allied Health Sciences, De Montfort University, Leicester, UK; <sup>3</sup>Laboratory of Cellular Metabolism, Department of Biochemistry, <sup>4</sup>Laboratory of Biochemistry of Lipids and <sup>5</sup>Laboratory of Neurobiology, Nencki Institute of Experimental Biology, Warsaw, Poland, <sup>6</sup>Department of Immunology, Medical University of Warsaw, Poland, <sup>7</sup>Laboratory of Molecular Basis of Behavior, Nencki Institute of Experimental Biology Warsaw, Poland; <sup>8</sup>School of Mechanical and Design Engineering, <sup>9</sup>School of Earth & Environmental Sciences and <sup>10</sup>Centre for Enzyme Innovation, University of Portsmouth, UK, <sup>11</sup>Military Institute of Hygiene and Epidemiology, Warsaw, Poland.

Running title: Calcification in dystrophin-null muscle

§Correspondence should be addressed to: Dariusz C. Górecki, M.D., Ph.D., Professor of Molecular Medicine, Tel: +44 (023) 9284 3566 (office), +44 (023) 9284 3616 (lab); Fax: +44 (023) 9284 3565; E-mail: [darek.gorecki@port.ac.uk](mailto:darek.gorecki@port.ac.uk)

**Keywords:** DMD, *mdx*, *mdx* <sup>$\beta$ geo</sup>, dystrophin, ectopic calcification, macrophages, skeletal muscle

---

### Funding

This work was supported by the Research and Innovation Development Fund, University of Portsmouth to DCG, the Muscular Dystrophy Association USA (MDA294571) to DCG, the Polish Ministry of National Defense project "Kościuszko" no: 523/2017/DA to DCG, a VC's Early Career Fellowship, De Montfort University, Leicester to CY, the National Science Centre, Poland, grant number: 2016/23/N/NZ4/03313, 2018/28/T/NZ4/00012 to LB and 2018/29/B/NZ4/02440 to KZ; Polish Ministry of Science and Higher Education grant number DI2016 007446 to PM.

Disclosures: None declared

## ABSTRACT

Duchenne muscular dystrophy (DMD) causes severe disability and death of young men due to progressive muscle degeneration aggravated by sterile inflammation. DMD is also associated with cognitive and bone-function impairments. This complex phenotype results from the cumulative loss of a spectrum of dystrophin isoforms expressed from the largest human gene. While there is evidence for the loss of shorter isoforms having impact in the CNS, their role in muscle is unclear. We found that at 8 weeks, the active phase of pathology in dystrophic mice, dystrophin-null mice (*mdx<sup>βgeo</sup>*) presented with a mildly exacerbated phenotype but without an earlier onset, increased serum CK levels or decreased muscle strength. However, at 12 months, *mdx<sup>βgeo</sup>* diaphragm strength was lower while fibrosis increased, compared to *mdx*. The most striking features of the dystrophin-null phenotype were increased ectopic myofibre calcification and altered macrophage infiltration patterns, particularly the close association of macrophages with calcified fibres. Ectopic calcification had the same temporal pattern of presentation and resolution in *mdx<sup>βgeo</sup>* and *mdx* muscles despite very significant intensity differences across muscle groups. Comparison of the rare dystrophin-null patients against those with mutations affecting full-length dystrophins only appears warranted.

## INTRODUCTION

Duchenne muscular dystrophy (DMD) is a severely debilitating and invariably fatal X-linked neuromuscular disorder, which results from mutations in the *DMD* gene<sup>1</sup>. *DMD* is the largest human gene known, encoding multiple structurally diverse isoforms of dystrophin<sup>2</sup>. Three full-length transcripts comprising 79 exons, encode 427 kDa proteins while further intragenic promoters<sup>3</sup> drive expression of progressively truncated variants (Figure 1A).

The current central hypothesis states that Duchenne muscular dystrophy pathology is caused by the loss of the full-length dystrophin (Dp427) in myofibres, where it anchors the dystrophin-associated protein complex (DAPC), linking the extracellular matrix, the sarcolemma and the intracellular cytoskeleton. This assembly is considered critical for muscle function and survival. Therefore, all the current pre-clinical and clinical therapeutic approaches are aimed at dystrophin restoration in differentiated muscle cells.

However, there is growing evidence that DMD mutations produce a range of significant cell-autonomous abnormalities in both human and mouse myogenic cells, suggesting a much earlier onset of pathology and explaining impaired muscle regeneration<sup>4-10</sup>.

The severity of DMD-associated cognitive impairment correlates with the cumulative loss of dystrophin isoforms expressed in the CNS, thus suggesting a prominent functional role for these shorter isoforms in brain cells<sup>11,12</sup>. However, little attention has been given to the potential role of shorter dystrophins controlled by the intergenic promoters and few in-depth comparisons between the full-length and the dystrophin-null muscle phenotypes have been undertaken. Interestingly, the proportion of patients with a severe motor and cognitive phenotype has been shown to correlate with mutations affecting all dystrophins<sup>13</sup>. Gene mutations causing DMD disrupt the reading frame and include large deletions (68%), duplications (11%) and also smaller re-

arrangements and point mutations (20%)<sup>14</sup>. Initial analyses indicated that the *DMD* gene mutation hotspots are located in the regions encoding the full-length isoforms. However, while large deletions and duplications have indeed a non-random distribution with the two identifiable hotspots, small insertions/deletions and point mutations are distributed along the entire gene<sup>15</sup> thus affecting multiple isoforms.

Interestingly, there is little data documenting the expression of the so-called 'non-muscle' dystrophin isoforms in muscle. Given that myogenic cells are affected by *DMD* mutations and are also known to express some of these truncated isoforms (e.g. Dp71), we hypothesized that null *DMD* mutations may alter functions of myogenic cells and thus affect the phenotype. Therefore, we investigated the consequences of total loss of *DMD* expression. We have compared the muscle pathology in the most widely used animal model of *DMD* - the *mdx* mouse, lacking full length isoforms due to point mutation in exon 23<sup>16</sup>, against the *mdx* <sup>$\beta$ geo</sup> dystrophin-null mouse with the reading-frame disruption downstream of exon 63, which is present in all dystrophins and therefore with all isoforms being ablated. This mouse, unlike models generated by chemical mutagenesis, is a true pan-dystrophin knockout with no revertant fibres present<sup>17</sup>.

## **MATERIALS AND METHODS**

### **Animals**

The male *mdx*, *mdx* <sup>$\beta$ geo</sup> wild type (Wt) control mice (C57B110 and C57B16 respectively) were used in accordance with institutional Ethical Review Board and the Home Office (UK) Approvals. The C57B110 and C57B16 strains derived from the common origin<sup>18</sup> and it has been demonstrated that the *mdx* mutation on the C57B16 background shows the same pathology as the original B110 strain<sup>19</sup>. All mice were maintained under pathogen-free conditions and in a controlled environment (12hr light/dark cycle, 19-23°C ambient temperature, 45-65% humidity). Mice were killed by CO<sub>2</sub> inhalation and cells and muscles dissected and used for protein extraction, or frozen in isopentane pre-chilled in liquid nitrogen for cryosectioning.

### **Antibodies and reagents**

The following antibodies were used at 1:1000: anti-dystrophin (ab15277, Abcam, Cambridge, UK) anti-actin (A2066, Sigma-Aldrich, Gillingham, UK), anti-F4/80 (Abcam, ab6640) and anti-CD68 (ab125212, Abcam). All other chemicals were purchased from Sigma or Fisher Scientific (Loughborough, UK).

### **Serum creatine kinase (CK) level measurement**

Blood samples were collected, allowed to coagulate and centrifuged for 10 minutes at 2500g. Sera isolated immediately after centrifugation were analyzed for the CK levels using the Creatine Kinase Activity Assay Kit (Mak116-1kt, Sigma), according to manufacturer's instructions.

### **Force measurements in diaphragms *ex vivo***

Whole diaphragms from 4 month Wt and dystrophic mice were excised and contractile force strength measured following the TREAT-NMD standard operating procedures (<http://treat->

nmd.eu/research/preclinical/dmd-sops/) and as previously described<sup>8</sup>. Essentially, diaphragms were placed into Krebs-Ringer solution. Sutures were tied and muscle then attached to an immobile plastic clamp with the central triangular section of the diaphragm being used for testing. Contractile force was measured using a mechanical force transducer (ADInstruments, Oxford, UK), amplifier, and data acquisition setup. Excitation was achieved via local field potentials through platinum electrodes in oxygenated (95% O<sub>2</sub>, 5% CO<sub>2</sub>) Krebs-Ringer solution, at a constant temperature (37°C). Following incremental stretching to establish the optimal excitation-to-force generation length and confirmation of the appropriate voltage twitch stimulus, diaphragm sections were subjected to a 140 V (2 ms) stimulus train at 100-Hz frequency for 0.5–1 s. The test regime involved collecting six twitch responses, followed by six tetanic trains, with a 2-min rest period between each. All forces were normalized to muscle wet weight and expressed as Newtons per gram of tissue (N/g).

### **Grip strength test**

In this and all other *in vivo* tests, investigators were blinded with respect to the sample group allocation. The grip strength test was performed as previously described<sup>20</sup> and according to the Treat NMD protocol ([http://www.treat-nmd.eu/downloads/file/sops/sma/SMA\\_M.2.1.002.pdf](http://www.treat-nmd.eu/downloads/file/sops/sma/SMA_M.2.1.002.pdf)). Essentially, mice were held by the tail and slowly approached to a metallic grid (6 × 6 cm) connected to a force sensor gauge (FG-5000A, Lutron Electronic, London, UK). Once the animal gripped the grid by its forelimbs, a gentle horizontal traction was applied to the tail until the animal let the grid go. The maximal force was recorded over two trials with a 1-min inter-trial interval. Strength was estimated by the mean of both trials.

### **RNA-Seq analysis**

Total RNA was extracted from tibialis anterior of 7 week old C57BL/10 and *mdx* male mice (n=4), quality controlled and sequenced as previously described<sup>8</sup>.

Quality control of raw reads was performed using fastQC (<http://www.bioinformatics.babraham.ac.uk/projects/fastqc/>). Reads were trimmed using trim-galore ([https://www.bioinformatics.babraham.ac.uk/projects/trim\\_galore/](https://www.bioinformatics.babraham.ac.uk/projects/trim_galore/)) with parameters to remove adapter sequence and low-quality sequence tails. Trimmed reads were mapped against the GRCm38 *Mus musculus* genome from Ensembl using the STAR universal RNA seq aligner<sup>21</sup> with the following parameters “--outSAMmultNmax 300 --outSAMstrandField intronMotif?”. Properly paired reads that mapped uniquely to the genome, with a mapping quality greater than 20, were retained for further analyses.

Differential expression analysis was conducted using the DESeq2 package<sup>22</sup> in R (<http://www.R-project.org/>). Gene models were taken from Ensembl version 91, and read counts over unique genes were quantified using the *summarizeOverlaps()* function in the GenomicAlignments package<sup>23</sup> using parameters ‘mode = “Union”, singleEnd = FALSE, ignore.strand = FALSE, fragments = FALSE, preprocess.reads = “invertStrand”’. P values were adjusted for multiple testing by using the Benjamini and Hochberg false discovery rate correction<sup>24</sup>. The whole muscle RNA seq data can be accessed from Array Express with the Accession Code E-MTAB-7698: <https://www.ebi.ac.uk/arrayexpress/experiments/E-MTAB-7698/>

## **Histological stains**

H&E, Alizarin Red, Periodic Acid Schiff, Von Kossa, Oil Red O and PicroSirius Red staining methodologies followed standard operating procedures from TREAT-NMD-recommended protocols available online (<http://treat-nmd.eu/research/preclinical/dmd-sops/>). All staining was carried out using 10- $\mu$ m-thick cryosections, air-dried onto poly-L-lysine coated glass slides (Fisher Scientific). Slides were mounted in DPX or aqueous media, coverslipped and imaged (Axiozoom V.16, Zeiss). Representative images per genotype are shown while montages, where  $n = 30$ -40, were constructed and assessed using pre-existing ImageJ (Fiji; ImageJ2: <https://fiji.sc/>) counting tools<sup>25</sup>.

## **Whole-body tissue clearing, imaging and analysis**

Clearing procedure was performed as described previously<sup>26</sup>. Briefly, animals were deeply anesthetized with intraperitoneal injection of lethal dose of sodium pentobarbital (100 mg/kg), subjected to cardiac perfusion, and fixation followed by 2-3 days of clearing with CUBIC reagent-1<sup>27</sup> or reagent-1A (deposited on <http://cubic.riken.jp> by Ueda and Susaki) clearing solutions and 1 day of 0,03% (wt/vol) AR staining dissolved in fresh clearing solution. Finally, specimens were placed for 2-3 days of gentle shaking with fresh clearing solution at 37°C in an incubator to remove the excess of unbound AR. Images were collected with customized light-sheet apparatus and analyzed according to also already described protocol<sup>26</sup>.

## **Immunolocalisation and morphological analyses**

Frozen muscle was transferred to a cryostat chamber and allowed to equilibrate to -20°C. Cryosections 10- $\mu$ m thick were then cut from the middle third of the sample and collected on poly-L-lysine (0.5 mg/ml)-coated glass slides. Sections were allowed to air dry for several hours. Samples were fixed in a 2%–4% w/v paraformaldehyde solution in TBST for 15 min at 4°C, followed by two washes in PBST. The primary antibody incubation in PBST containing 10% v/v serum was applied for 2 h at room temperature or overnight at 4°C. Three 5-min TBST washes were applied before secondary antibody incubation in PBST and 10% v/v serum containing Hoechst (1:1000) fluorescent nuclear counterstain for 1 h at room temperature. Sections were finally washed three times for 30 min before mounting in FluorSave (Merk Millipore, Watford, UK) fluorescence mounting medium. Either entire cross sections through the mid-portion of TA muscles were captured in their entirety using Axiozoom V.16 (Zeiss), or whole cross-sections were made of montaged 20 $\times$  magnification fields of view. For quantification of immunofluorescent cells, a semi-automated (unbiased) method using a thresholding macro designed in ImageJ was used. Numbers were then expressed per unit of area. For diaphragms, counts per unit area for each animal were derived by averaging the counts from five fields of view encompassing a significant portion of each diaphragm cross-section. Counts were also made using the threshold and *analyse particles* functions of ImageJ.

## **Western blotting**

Proteins were extracted, resolved and blotted as described previously<sup>20,28</sup>. Blots were blocked in 5% w/v non-fat milk powder in 1x Tris buffered saline (TBST; 50 Mm Tris, 150 mM NaCl, 0.01% v/v Tween-20,

Sigma), for 1 h prior to probing with primary antibody diluted in the same blocking buffer (overnight at 4°C or 2 h at room temperature), then washed (3 times) with 1 x TBST for 10 min and incubated with the appropriate horseradish peroxidase-conjugated secondary antibody; anti-mouse 1:10:000 (Sigma, A4416), anti-rabbit 1:5000 (Sigma, A6154) overnight at 4°C or 1 h at room temperature. Specific protein bands were visualized using Luminata Classico or Forte chemiluminescent substrates (Merck Millipore, WBLUC0500 and WBLUF0500, respectively), images were obtained using a ChemiDoc MP system (Bio-Rad, Hertfordshire, UK). Densitometric analyses were performed using the integrated density measurement function of ImageJ software. All experiments were repeated at least 3 times in triplicate, throughout.

### **X-ray micro computed tomography**

Quadriceps were placed within a 1.5 mL tube (Eppendorf, EU) and supported by a polyurethane foam saturated in 70% ethanol. Muscles were imaged using a Zeiss Xradia 520 Versa X-ray microscope (Zeiss, Cambridge, UK) operating at an energy of 50 kV, a power of 4 W, a tube current of 80  $\mu$ A and a Zeiss LE1 filter was positioned directly after the X-ray source. A 0.4x objective lens was used with an X-ray source – sample distance of 20 mm and a detector – sample distance of 105 mm. One thousand six hundred and one X-ray projection images were collected over 360° at equal intervals with an isotropic voxel size of 11  $\mu$ m. The exposure time for each projection was 2 s. The projections were reconstructed using the manufacturer's integrated software which utilizes a filtered back projection reconstruction algorithm. The individual tomography scans were quantified in using the threshold function in ImageJ<sup>25</sup> and visualized in 3D using TXM3DViewer (Zeiss).

### **Statistical analysis**

Results are reported as means +/- SD where n refers to number of independent experiments (3-6). Significance scores were based on Kruskal-Wallis with post-hoc Dunn's test for non-parametric multiple comparisons; one-way ANOVA with post-hoc Tukey test for normal multiple comparisons; un-paired t-tests for individual comparisons, with Mann Whitney post-hoc test for non-parametric t-tests (GraphPad Prism8). For cumulative frequency distribution Kolmogorov-Smirnov test was used. Differences were considered statistically significant at P <0.05.

## **RESULTS**

### **Dystrophic pathology in *mdx*<sup>*fl<sup>geo</sup>*</sup> dystrophin-null mice.**

Muscle pathology in the *mdx* muscles begins to present at 2-3 weeks, reaching maximum intensity in leg muscles at about 8 weeks, before plateauing around 12-16 weeks<sup>29,30</sup>. However, the *mdx* mouse diaphragm shows progressive pathology<sup>31</sup> and therefore this muscle closely represents the human condition.

To identify the potential phenotypic differences resulting from the absence of all vs. full length isoforms we compared *mdx* and *mdx*<sup>*fl<sup>geo</sup>*</sup> (dystrophin null) mice (Figure 1) following the TREAT-NMD standard operating procedures<sup>32,33</sup>.

At 8 weeks (the peak of pathology), morphological analysis of leg muscles revealed a significant shift in myofibre cross-sectional area towards smaller fibres in dystrophic muscle in the order of Wt (BL10) > *mdx* > *mdx* <sup>$\beta$ geo</sup> (Figure 2A & B). A significant reduction in the average ferret diameter followed the same trend (Figure 2C, Kruskal-Wallis with Dunn's test,  $P < 0.0001$ ). Central nucleation was significantly elevated in *mdx* <sup>$\beta$ geo</sup> compared to *mdx* (Figure 2D, Mann-Whitney test,  $P = 0.0159$ ). At 8 weeks, serum CK levels (Figure 2E) were not significantly different (Mann-Whitney test,  $P = 0.4127$ ) between the two dystrophic strains, indicating that loss of short dystrophins did not exacerbate sarcolemma damage. Grip strength *in vivo* (Figure 2F) and diaphragm strength *ex-vivo* (Figure 2G) were equally reduced in both dystrophic strains at 8 weeks. Yet, there was an age-dependent difference between *mdx* <sup>$\beta$ geo</sup> and *mdx*: In 12-month-old animals diaphragm contractile force strength showed small but significant increase in *mdx* preparations (unpaired t test,  $t = 6.572$ ,  $df = 4$ ,  $P = 0.0028$ ), but no increase was found in *mdx* <sup>$\beta$ geo</sup> (Figure 2G, unpaired t test,  $t = 0.6558$ ,  $df = 4$ ,  $P = 0.5478$ ). Furthermore, fibrosis (Figure 2I) and fat accumulations (Figure 2J) were both found elevated in 12-month-old *mdx* <sup>$\beta$ geo</sup> diaphragms compared to age matched *mdx*.

### **Total dystrophin loss exacerbates ectopic calcification of dystrophic muscle fibres**

Muscles from *mdx* <sup>$\beta$ geo</sup> mice do not express any dystrophin isoforms (Figure 1B) nor truncated variants in revertant fibres (Figure 3A). In contrast, at 8 weeks, striking opaque fibres, particularly prominent in diaphragms but detectable in all major skeletal muscle groups, were found to be notably more abundant in *mdx* <sup>$\beta$ geo</sup> than in *mdx* mice (Figure 3B-D). The appearance of these fibres closely resembled ectopic calcification reported previously in the *mdx*, *mdx/Utrophin* double knock-out and the humanized-*mdx* mouse models<sup>34-37</sup>, in the GRMD dog<sup>38,39</sup> and, importantly, DMD patients<sup>40</sup>. To confirm, we first verified the presence of calcium- and phosphorus-containing deposits in these opaque diaphragm fibres using Alizarin red (AR) (Figure 4A) and Von Kossa (Figure 4B) stains, respectively. SEM energy-dispersive X-ray spectroscopy electron back-scatter analysis (Figure 4C) confirmed the presence of mineral deposits containing both calcium (Figure 4D) and phosphate (Figure 4E) with a molar ratio of Ca:P of 3:2 (Figure 4F), consistent with tricalcium phosphate  $[\text{Ca}_3(\text{PO}_4)_2]$ <sup>41</sup>.

The striated appearance of calcified fibres showed regions of calcification with distinct patterning, sometimes along the length of almost entire fibre, sometimes in short regions of otherwise unaltered fibre (Figure 3C, right panel [arrowed] & Supplementary Video 1). Muscle groups most severely affected with ectopic calcification were diaphragm (Figure 3B) and the proximal limb (*quadriceps* and *gluteus*) with a consistently milder phenotype in the distal groups (*tibialis anterior* (TA) and *gastrocnemius* (GC), Figure 3C). Importantly, this ectopic calcification was also found in cardiac muscles of *mdx* <sup>$\beta$ geo</sup> (Figure 3D and Supplementary Figure 1) which, to our knowledge, is the first demonstration of this abnormality in a DMD model.

### **Whole body musculature analysis of ectopic calcification in *mdx* and *mdx* <sup>$\beta$ geo</sup>.**

The initial study revealed very significant differences in ectopic calcifications between various muscle groups, indicating the need for systematic comparisons. To screen for and quantify ectopic mineralization in various muscle groups of the entire animal we have applied previously optimized whole-body tissue optical clearing methodology<sup>26</sup>. Such an approach, when combined with AR staining, allowed us to demonstrate excessive accumulation of ectopic calcifications in *mdx* <sup>$\beta$ geo</sup> vs. *mdx* and confirm complete absence of these in control animals (Figure 5A-D). Thereby, we observed calcified deposits particularly abundant within *mdx* <sup>$\beta$ geo</sup> diaphragms (Figure 5B) but also in skeletal muscles of the laryngopharynx, forelimb, lumbar region, pelvic region, and hind limbs. Next, we utilized a customized light-sheet setup to perform detailed three-dimensional imaging of isolated muscles from three distinct body regions i.e. *spinalis pars lumborum*, *biceps femoris* and *triceps brachii*, (Figure 5E-F). When compared to *mdx*, every *mdx* <sup>$\beta$ geo</sup> muscle was characterized by a higher percentage of tissue mineralization, differences being particularly striking in *triceps brachii*, where ectopic calcification reached 11.59% in *mdx* <sup>$\beta$ geo</sup> and 0.36% in *mdx* (Figure 5F: percent of mineralization: unpaired t-test  $t(4) = 5.32$   $P < 0.01$ ). In contrast, the difference was not found statistically significant in *spinalis pars lumborum* (Figure 5F: unpaired t-test  $t(4) = 2.62$   $p = 0.058$ ) and *biceps femoris* (Figure 5F: unpaired t-test  $t(4) = 0.97$   $p = 0.386$ ). Cumulative frequency distribution analysis showed different distribution of calcified deposits in *triceps brachii* and *spinalis pars lumborum* muscles from *mdx* <sup>$\beta$ geo</sup> mice in comparison to *mdx* mice (Figure 5F).

Further confirmation of muscle fibre calcifications was undertaken using AR staining of *tibialis anterior* (TA) (Figure 6C & D) and diaphragm (Figure 6A & B) sections and particle analysis-based quantification of thresholded images using ImageJ (Figure 6E). Significantly elevated numbers and percentages of calcified fibres were confirmed in diaphragms (Figure 6F) while TA was confirmed to be less affected by the ectopic calcification. Finally, ectopic calcifications in isolated 8 week old *quadriceps mdx* and *mdx* <sup>$\beta$ geo</sup> muscles were visualized in 3D under the X-ray microscope (Zeiss, Xradia, Figure 6G-J and also see Supplementary Video 1).

### **Age of onset and evolution of ectopic muscle mineralization in *mdx* and *mdx* <sup>$\beta$ geo</sup>.**

The onset and progression of muscle pathology in the *mdx* muscle are well documented with cycles of degeneration and regeneration and significant sterile inflammation between 3 and 12 weeks of age, followed by a significant reduction of symptoms from 12 weeks onwards. The exception is diaphragm, where the pathology is progressive and thus resembles human disease<sup>29,30</sup>. Aforementioned exacerbation of ectopic mineralization in *mdx* <sup>$\beta$ geo</sup> led us to assess whether total dystrophin ablation triggers an earlier onset of dystrophic damage with ectopic calcification. To test this hypothesis, we analyzed AR staining intensities in 2 and 4-week-old *mdx* and *mdx* <sup>$\beta$ geo</sup> diaphragm muscle sections. We found 2 week muscles to be visually devoid of detectable calcifications (Figure 7A-C), but at 4 weeks white striations were clearly beginning to form in limb and diaphragm muscles (Figure 7D-F). Quantification of AR staining in diaphragm sections confirmed first calcified fibres to appear somewhere between 2-4 weeks of age but equally in both *mdx* and *mdx* <sup>$\beta$ geo</sup> animals (Figure 7J). Given the nature of the ectopic calcification, it could be expected to worsen with



age, particularly in diaphragms. However, analyses in 3 month and 6 month old mice showed the calcified fibres could no longer be found (Figure 7K). The diaphragm appearance, with thickening and opacity (Figure 7H-I) may be due to ongoing inflammation and emerging fibrosis, which are pathological hallmarks of 12-month-old diaphragms. Indeed, PicroSirius Red staining for collagen (Figure 2H) revealed the presence of fibrosis.

### **Differences in macrophage distribution and association with mineralized fibres in *mdx* vs. *mdx*<sup>*βgeo*</sup> diaphragms.**

Inflammation is the well-known pathological hallmark of DMD. It affects muscle regeneration but also degeneration and fibrosis<sup>42,43</sup>. Of the inflammatory cells found in *mdx* muscles, macrophages play a very significant yet complex role: Their depletion results in the reduction or exacerbation of pathology depending on the stage of disease<sup>43,44, 34</sup>. Our RNASeq data (Array Express Code E-MTAB-7698) identified very significant contribution of macrophage genes to the altered inflammatory gene expression profile in *mdx* muscles (Supplementary Figure 2). Furthermore, a recent study has demonstrated that inorganic phosphate can specifically activate macrophages to prevent ectopic calcification<sup>45</sup>. Given that the evolution of calcified muscle fibres mirrored the onset and cessation of inflammation in *mdx* muscle, we analyzed the immune cells in muscle sections. F4/80 staining for macrophages was markedly different in the two dystrophic strains: *mdx* muscle showed scattered staining with numerous macrophage puncta spread throughout the tissue and only some larger puncta of intense staining (Figure 8C & G). In contrast, *mdx*<sup>*βgeo*</sup> muscles displayed large F4/80 positive puncta, which co-localised perfectly with mineralized fibres and appeared almost uniquely and intricately associated with them (Figure 8A, B, D, E, F & H). Often, macrophages were tightly associated with what appeared to be partially degraded fibres (Figure 8B, arrowed). The CD68 and osteopontin staining co-localisation in these macrophages indicated their predominantly M1 phenotype (Figure 8J & K).

In conclusion, we have found that total loss of dystrophin expression in the mouse model of DMD specifically exacerbates ectopic myofibre calcification, alters macrophage infiltration and aggravates the subsequent fibrosis.

## **DISCUSSION**

There is evidence that absence of the full-length (427 kDa) dystrophin in the fully-differentiated myofibres may not necessarily cause the dystrophic phenotype<sup>46,47</sup>. In contrast, Dp427 has been shown to play a role in satellite cells<sup>4,5,9,48,49</sup> and there are clear data that a lack of DMD gene expression affects various important functions of myoblasts, including cell proliferation, differentiation, energy metabolism and signaling<sup>6,8,50</sup>. These and other findings indicate that dystrophic pathology starts much earlier than has been suggested<sup>51</sup> and point at the importance of the loss of dystrophin expression in myogenic cells, dysfunction of which determines abnormalities of muscle regeneration and therefore disease progression. Given that the Dp71 dystrophin has been found in undifferentiated myogenic cells<sup>52</sup> we hypothesized that *Dmd* gene mutations eliminating expression of this isoform may further alter functions of myogenic cells and thus affect the

dystrophic phenotype. Therefore, we have compared the muscle pathology in the most widely used animal model of DMD - the *mdx* mouse, lacking full length isoforms due to a stop mutation in exon 23<sup>16</sup>, against the *mdx<sup>βgeo</sup>* dystrophin null mouse<sup>17</sup>. The latter DMD model is interesting as it has no observed dystrophin positive revertant fibre clusters<sup>44</sup> and also allows complex phenotypes to be investigated. Notably, mutation hotspots of large deletions and duplications are located in the regions encoding the full-length isoforms. However, small insertions/deletions and point mutations are distributed along the entire gene<sup>15</sup> and these would affect the full spectrum of dystrophins. However, there is little data evaluating the role of the shorter dystrophin isoforms in muscle.

Our analyses revealed a slightly exacerbated phenotype in *mdx<sup>βgeo</sup>*, especially in older mice. However, these dystrophin-null mice did not show an earlier onset of the dystrophic pathology, which might have been expected given that Dp71 was found expressed in muscle development<sup>17,53</sup>. The muscle pathology being similar to that in *mdx* mice was in agreement with the previous study in Cre-loxP mouse, in which DMD gene was deleted<sup>54</sup>. Moreover, no increase in serum CK levels, indicative of sarcolemma permeability, suggested a different role for this short isoform. Interestingly, the most striking alteration in *mdx<sup>βgeo</sup>*, was the ectopic calcification. Ectopic calcifications have been reported previously in *mdx*<sup>34,55</sup> and were found particularly abundant in *mdx/Utrrophin* dKO, *mdx/δ-sarcoglycan* dKO<sup>56</sup> and the humanized-*mdx* mouse models<sup>34-37</sup>, which all present with an exacerbated dystrophic phenotype. Notably, ectopic calcifications are also found in human DMD patients<sup>40</sup>.

One explanation for the different phenotypes could be the protection afforded to the *mdx* muscle by the revertant, dystrophin positive fibres. These revertants are thought to arise through splicing events, and occur at varying frequencies in different muscle groups; approximate average values of 2-7% in TA and 1-4% in diaphragm have been reported previously in the *mdx* mouse<sup>57</sup>. These fibres are completely absent from *mdx<sup>βgeo</sup>* muscles. Given that ~15% dystrophin-positive fibres appear sufficient to protect against contraction-induced injury<sup>58</sup>, revertant fibres could perhaps have some impact.

Another important question is: which cells are affected by the lack of short dystrophins? Given that myofibres do not express Dp71, it is likely that these are satellite cells or myoblasts. However, the loss of DMD gene expression in non-muscle cells cannot be excluded, as indicated by the purinergic phenotype found in DMD patients' lymphoblasts<sup>59</sup>. Therefore, disease phenotypes in DMD patients with mutation affecting all dystrophins should be re-evaluated.

Importantly, there were very significant differences in ectopic calcifications between different muscle groups. This finding may shed new light on the mechanism behind the absence of damage in some and the progressive pathology in other muscle groups that are observed in both DMD patients and mouse models of this disease. This diversity in ectopic calcification was confirmed using a combination of methods including X-ray microscopy and our newly developed whole-body optical tissue clearing approach<sup>30</sup>. The latter method allows to perform highly reproducible and quantitative assessment of mineralization without a need for highly specialized and expensive equipment thus permits such unbiased complete comparisons to be performed in numerous laboratories. SEM energy-dispersive X-ray spectroscopy electron back-scatter analysis of mineralized fibers revealed the presence of calcium and phosphate with a molar ratio of 3:2, consistent with

tricalcium phosphate  $[\text{Ca}_3(\text{PO}_4)_2]$ <sup>34</sup>. NMR-based approaches would be more conclusive but difficulties in obtaining entirely organic-free material without sample damage prevented further investigations. Therefore, while the presence of hydroxyapatite previously described in *mdx* muscle cannot be ruled out, this material was reported between rather than within fibres, what was documented here<sup>34</sup>.

Calcified muscles have been linked to increased inorganic phosphate (Pi) levels and serum Pi was found elevated in *mdx* mice<sup>45</sup>. Furthermore, dietary Pi intake has been shown to increase muscle calcifications while reduced Pi diet alleviated ectopic calcifications in *mdx* mouse muscle in vivo<sup>44,60</sup>. In turn, calcium precipitate inhibition with pyrophosphate and bisphosphonate have already showed therapeutic promise in DMD<sup>61-63</sup>. However, it is not clear whether ectopic calcification is linked to the intracellular calcium accumulation, which resulted in the “calcium hypothesis” of DMD damage. Assuming that these events are connected, the exacerbated calcification in the dystrophin-null muscle suggests that the calcium influx via permeable sarcolemma solely due to the absence of Dp427 is an insufficient explanation<sup>64</sup>. Indeed, while elevated calcium levels in muscle fibres are sufficient to induce dystrophic-like changes<sup>65</sup>, this can occur independently of membrane instability<sup>66</sup>.

Ectopic calcification was also found in *mdx*<sup>*βgeo*</sup> hearts but without obvious histological deterioration compared to *mdx*. This data also agree with observations of cardiac histopathology not being significantly different between *mdx* and the Cre-loxP DMD null mice<sup>12</sup>. Interestingly, Dp71 in cardiomyocytes is located exclusively to the T-tubules<sup>12</sup>. Given that the majority of the calcium enters the cell via T-tubules, absence of Dp71 could affect this function and contribute to ectopic calcification.

Ectopic calcifications in dystrophic muscle appeared at 3-4 weeks in both *mdx* and *mdx*<sup>*βgeo*</sup> mice, increasing in number up until 8-12 weeks, beyond which calcified myofibres were replaced by fibrosis, which is one of the hallmarks of this disease. Thus, calcification follows the course of *mdx* pathology in limb muscles and in the diaphragm, one *mdx* muscle that most closely reproduces disease progression in humans. The timing of calcified fibres being replaced by fibrosis was also around week 12. Therefore, calcification seems to have the same temporal pattern of presentation and resolution in all dystrophic muscle despite very significant differences in intensity across different muscle groups (see Fig 5).

The cycles of degeneration and regeneration in *mdx* muscle are concomitant with immune cell infiltrations. These immune cells are attracted by the DAMPs released from damaged muscle and they play important roles in the pathology: They can contribute to damage but are also involved in clearing the cellular debris and releasing factors facilitating satellite cell activation and therefore promoting muscle regeneration. Moreover, in the chronic disease, inflammation is also linked to fibrosis<sup>31,32</sup>.

The role of macrophages in these processes has been well-documented: Pathology in immunocompromised *mdx* mice that retained functional macrophages was largely unaltered<sup>33</sup>, whereas macrophage depletion before the onset of muscle damage resulted in significant improvement<sup>34,35</sup> while total ablation exacerbated the disease<sup>43</sup>. Furthermore, a recent study demonstrated that inorganic phosphate can activate macrophages to adopt a phenotype allowing them to prevent ectopic calcification<sup>36</sup>. Given that the evolution of calcified muscle fibres mirrored the onset and cessation of inflammatory cell infiltrates in *mdx* muscle and the important role of macrophages, we analyzed these cells in relation to calcification. The distribution of macrophages was

markedly different in *mdx* vs. *mdx*<sup>*βgeo*</sup> muscles, with a very close co-localisation of F4/80 staining puncta with mineralized fibres in the latter. Moreover, the staining often appeared crescent-shaped, around what looked like partially digested fibres (Figure 8B, arrow). In view that that Pi-induced macrophages can evoke anti-calcification actions, which are mediated by increased availability of extracellular ATP and pyrophosphate<sup>36</sup>, the dystrophic muscle would offer ideal conditions for their activation. However, markers expressed on cells in *mdx*<sup>*βgeo*</sup> muscles suggested that these had predominantly the M1 phenotype while the Pi induces macrophages were shown to adopt a phenotype resembling the M2 subtype<sup>36</sup>. Of course, macrophages are known for their ability to change phenotype in response to environmental signals so functional interplay between populations preventing calcification and eliminating calcified deposits is possible. Manipulating macrophage functions should provide further insight into their role in this process.

Understanding these phenomena may also aid in identifying new therapeutic approaches. Furthermore, ectopic calcifications are associated with pathological outcomes in many human disorders apart from DMD, including osteoarthritis<sup>67</sup>, atherosclerosis<sup>60</sup>, sarcoma<sup>68</sup>, renal disease<sup>69</sup>, *fibrodysplasia ossificans progressiva*<sup>70</sup> and soft tissue impact trauma<sup>71</sup>, where macrophage-specific roles are already established.

Given our mouse model data and the correlation of severity of patients' cognitive impairment with the loss of shorter dystrophins both suggesting a prominent functional role for these isoforms, comparison of muscle pathology in dystrophin-null patients against those with mutations affecting full-length dystrophins only is clearly warranted. Mouse with selective ablation of Dp71 is not dystrophic<sup>53</sup> but presents with retinal channels abnormality<sup>72</sup>, early cataract formation<sup>73</sup> and vomeronasal nerve defasciculation<sup>74</sup>. In contrast, transgenic overexpression of Dp71 resulted in more severe muscle disease<sup>75,76</sup>. Therefore, it may not be the absence of Dp71 but altered expression of dystrophin isoforms at a critical time point or/and at a specific location that causes the pathology.

Understanding the mechanism of this abnormality may contribute to the development of more effective treatments not only for DMD but a range of diseases.

## Acknowledgments

The authors wish to thank Dr Slawomir Pikula for advice on mineral deposit analysis and Mr Scott Roadway for help with *in vivo* experiments.

## REFERENCES

1. Hoffman EP, Fischbeck KH, Brown RH, Johnson M, Medori R, Loire JD, Harris JB, Waterston R, Brooke M, Specht L, Kupsky W, Chamberlain J, Caskey CT, Shapiro F, Kunkel LM: Characterization of Dystrophin in Muscle-Biopsy Specimens from Patients with Duchenne's or Becker's Muscular Dystrophy. *N Engl J Med* 1988, 318:1363–1368.
2. Hoffman EP, Brown RH, Kunkel LM: Dystrophin: The protein product of the duchenne muscular dystrophy locus. *Cell* 1987, 51:919–928.
3. Ahn a H, Kunkel LM: The structural and functional diversity of dystrophin. *Nat Genet* 1993, 3:283–291.
4. Dumont NA, Wang YX, Von Maltzahn J, Pasut A, Bentzinger CF, Brun CE, Rudnicki MA: Dystrophin expression in muscle stem cells regulates their polarity and asymmetric division. *Nat*

- Med 2015, 21:1455–1463.
5. Dumont NA, Wang YX, Rudnicki MA: Intrinsic and extrinsic mechanisms regulating satellite cell function. *Development* 2015, 142:1572–1581.
  6. Yeung D, Zablocki K, Lien C-F, Jiang T, Arkle S, Brutkowski W, Brown J, Lochmuller H, Simon J, Barnard E a, Górecki DC: Increased susceptibility to ATP via alteration of P2X receptor function in dystrophic mdx mouse muscle cells. *FASEB J* 2006, 20:610–620.
  7. Young CNJ, Brutkowski W, Lien CF, Arkle S, Lochmüller H, Zablocki K, Górecki DC: P2X7 purinoceptor alterations in dystrophic mdx mouse muscles: Relationship to pathology and potential target for treatment. *J Cell Mol Med* 2012, 16:1026–1037.
  8. Young CNJ, Sinadinos A, Lefebvre A, Chan P, Arkle S, Vaudry D, Gorecki DC: A novel mechanism of autophagic cell death in dystrophic muscle regulated by P2RX7 receptor large-pore formation and HSP90. *Autophagy* 2015, 11:113–130.
  9. Yablonka-Reuveni Z, Anderson JE: Satellite cells from dystrophic (Mdx) mice display accelerated differentiation in primary cultures and in isolated myofibers. *Dev Dyn* 2006, 235:203–212.
  10. Blau HM, Webster C, Pavlath GK: Defective myoblasts identified in Duchenne muscular dystrophy. *Proc Natl Acad Sci* 1983, 80:4856–4860.
  11. Taylor PJ, Betts GA, Maroulis S, Gilissen C, Pedersen RL, Mowat DR, Johnston HM, Buckley MF: Dystrophin gene mutation location and the risk of cognitive impairment in duchenne muscular dystrophy. *PLoS One* 2010, 5:e8803.
  12. Masubuchi N, Shidoh Y, Kondo S, Takatoh J, Hanaoka K: Subcellular localization of dystrophin isoforms in cardiomyocytes and phenotypic analysis of dystrophin-deficient mice reveal cardiac myopathy is predominantly caused by a deficiency in full-length dystrophin. *Exp Anim* 2013, 213:36–47.
  13. Desguerre I, Christov C, Mayer M, Zeller R, Becane HM, Bastuji-Garin S, Leturcq F, Chiron C, Chelly J, Gherardi RK: Clinical heterogeneity of Duchenne muscular dystrophy (DMD): Definition of sub-phenotypes and predictive criteria by long-term follow-up. *PLoS One* 2009, 4:e4347.
  14. Aartsma-Rus A, Ginjaar IB, Bushby K: The importance of genetic diagnosis for Duchenne muscular dystrophy. *J Med Genet* 2016, 53:145–151.
  15. Juan-Mateu J, Gonzalez-Quereda L, Rodriguez MJ, Baena M, Verdura E, Nascimento A, Ortez C, Baiget M, Gallano P: DMD mutations in 576 dystrophinopathy families: A step forward in genotype-phenotype correlations. *PLoS One* 2015, 10:1–21.
  16. Bulfield G, Siller WG, Wight PA, Moore KJ: X chromosome-linked muscular dystrophy (mdx) in the mouse. *Proc Natl Acad Sci U S A* 1984, 81:1189–1192.
  17. Wertz K, Füchtbauer EM: Dmd(mdx- $\beta$ geo): A new allele for the mouse dystrophin gene. *Dev Dyn* 1998, 212:229–241.
  18. Petkov PM, Ding Y, Cassell MA, Zhang W, Wagner G, Sargent EE, Asquith S, Crew V, Johnson KA, Robinson P, Scott VE, Wiles M V.: An efficient SNP system for mouse genome scanning and elucidating strain relationships. *Genome Res* 2004, 14:1806–1811.
  19. McGreevy JW, Hakim CH, McIntosh MA, Duan D: Animal models of Duchenne muscular dystrophy: from basic mechanisms to gene therapy. *Dis Model Mech* 2015, 8:195–213.
  20. Al-Khalidi R, Panicucci C, Cox P, Chira N, Róg J, Young CNJ, McGeehan RE, Ambati K, Ambati J, Zablocki K, Gazzerri E, Arkle S, Bruno C, Górecki DC: Zidovudine ameliorates pathology in the mouse model of Duchenne muscular dystrophy via P2RX7 purinoceptor antagonism. *Acta Neuropathol Commun* 2018, 6:27.
  21. Dobin A, Davis CA, Schlesinger F, Drenkow J, Zaleski C, Jha S, Batut P, Chaisson M, Gingeras TR: STAR: Ultrafast universal RNA-seq aligner. *Bioinformatics* 2013, 29:15–21.
  22. Love MI, Huber W, Anders S: Moderated estimation of fold change and dispersion for RNA-seq data with DESeq2. *Genome Biol* 2014, 15:550–571.
  23. Lawrence M, Huber W, Pagès H, Aboyoun P, Carlson M, Gentleman R, Morgan MT, Carey VJ: Software for Computing and Annotating Genomic Ranges. *PLoS Comput Biol* 2013, 9:1–10.
  24. Hochberg B: Controlling the False Discovery Rate: a Practical and Powerful Approach to Multiple Testing. *J R Stat Soc* 1995, 57:289–300.
  25. Abramoff MD, Magalhães PJ, Ram SJ: Image processing with imageJ. *Biophotonics Int.* 2004, pp. 36–41.
  26. Bozycki L, Łukasiewicz K, Matryba P, Pikula S: Whole-body clearing, staining and screening of calcium deposits in the mdx mouse model of Duchenne muscular dystrophy. *Skelet Muscle* 2018, 8.
  27. Susaki EA, Tainaka K, Perrin D, Kishino F, Tawara T, Watanabe TM, Yokoyama C, Onoe H,

- Eguchi M, Yamaguchi S, Abe T, Kiyonari H, Shimizu Y, Miyawaki A, Yokota H, Ueda HR: Whole-brain imaging with single-cell resolution using chemical cocktails and computational analysis. *Cell* 2014, 157:726–739.
28. Sinadinos A, Young CNJ, Al-Khalidi R, Teti A, Kalinski P, Mohamad S, Floriot L, Henry T, Tozzi G, Jiang T, Wurtz O, Lefebvre A, Shugay M, Tong J, Vaudry D, Arkle S, DoRego JC, G?recki DC: P2RX7 Purinoceptor: A Therapeutic Target for Ameliorating the Symptoms of Duchenne Muscular Dystrophy. *PLoS Med* 2015, 12:1–33.
  29. Suelves M, Vidal B, Serrano AL, Tjwa M, Roma J, López-Alemaný R, Luttun A, De Lagrán MM, Díaz MÀ, Jardí M, Roig M, Dierssen M, Dewerchin M, Carmeliet P, Muñoz-Cánoves P: uPA deficiency exacerbates muscular dystrophy in MDX mice. *J Cell Biol* 2007, 178:1039–1051.
  30. Yucel N, Chang AC, Day JW, Rosenthal N, Blau HM: Humanizing the mdx mouse model of DMD: the long and the short of it. *npj Regen Med* 2018, 3:4.
  31. Stedman HH, Sweeney HL, Shrager JB, Maguire HC, Panettieri RA, Petrof B, Narusawa M, Leferovich JM, Sladky JT, Kelly AM: The mdx mouse diaphragm reproduces the degenerative changes of Duchenne muscular dystrophy. *Nature* 1991, 352:536–539.
  32. Aartsma-Rus A, van Putten M: Assessing functional performance in the mdx mouse model. *J Vis Exp* 2014, :e51303.
  33. Briguet A, Courdier-Fruh I, Foster M, Meier T, Magyar JP: Histological parameters for the quantitative assessment of muscular dystrophy in the mdx-mouse. *Neuromuscul Disord* 2004, 14:675–682.
  34. Kikkawa N, Ohno T, Nagata Y, Shiozuka M, Kogure T, Matsuda R: Ectopic calcification is caused by elevated levels of serum inorganic phosphate in mdx mice. *Cell Struct Funct* 2009, 34:77–88.
  35. Sohn J, Lu A, Tang Y, Wang B, Huard J: Activation of non-myogenic mesenchymal stem cells during the disease progression in dystrophic dystrophin/utrophin knockout mice. *Hum Mol Genet* 2015, 24:3814–3829.
  36. Greco N, Dong Q, Vo N, Kang J, Wang B: NIH Public Access. 2014, 31:343–349.
  37. Wada E, Yoshida M, Kojima Y, Nonaka I, Ohashi K, Nagata Y, Shiozuka M, Date M, Higashi T, Nishino I, Matsuda R: Dietary phosphorus overload aggravates the phenotype of the dystrophin-deficient mdx mouse. *Am J Pathol, American Society for Investigative Pathology*, 2014, 184:3094–3104.
  38. Barthélémy I, Uriarte A, Drougard C, Unterfinger Y, Thibaud JL, Blot S: Effects of an Immunosuppressive Treatment in the GRMD Dog Model of Duchenne Muscular Dystrophy. *PLoS One* 2012, 7:e48478.
  39. Liu JMK, Okamura CS, Bogan DJ, Bogan JR, Childers MK, Kornegay JN: Effects of prednisone in canine muscular dystrophy. *Muscle and Nerve* 2004, 30:767–773.
  40. Larcher T, Lafoux A, Tesson L, Remy S, Thepenier V, François V, Le Guiner C, Goubin H, Dutilleul M, Guigand L, Toumaniantz G, De Cian A, Boix C, Renaud J-B, Cherel Y, Giovannangeli C, Concordet J-P, Anegon I, Huchet C: Characterization of dystrophin deficient rats: a new model for Duchenne muscular dystrophy. *PLoS One* 2014, 9:e110371.
  41. Vallet-Regí M: Ceramics for medical applications. *J Chem Soc Dalt Trans* 2001, :97–108.
  42. Villalta SA, Rosenberg AS, Bluestone JA: The immune system in Duchenne muscular dystrophy: Friend or foe. *Rare Dis* 2015, 3:e1010966.
  43. Villalta SA, Nguyen HX, Deng B, Gotoh T, Tidbal JG: Shifts in macrophage phenotypes and macrophage competition for arginine metabolism affect the severity of muscle pathology in muscular dystrophy. *Hum Mol Genet* 2009, 18:482–496.
  44. Farini A, Meregalli M, Belicchi M, Battistelli M, Parolini D, D’Antona G, Gavina M, Ottoboni L, Constantin G, Bottinelli R, Torrente Y: T and B lymphocyte depletion has a marked effect on the fibrosis of dystrophic skeletal muscles in the scid/mdx mouse. *J Pathol* 2007, 213:229–238.
  45. Villa-Bellosta R, Hamczyk MR, Andrés V: Novel phosphate-activated macrophages prevent ectopic calcification by increasing extracellular ATP and pyrophosphate. *PLoS One* 2017, 12:e0174998.
  46. Seno MMG, Graham IR, Athanasopoulos T, Trollet C, Pohlschmidt M, Crompton MR, Dickson G: RNAi-mediated knockdown of dystrophin expression in adult mice does not lead to overt muscular dystrophy pathology. *Hum Mol Genet* 2008, 17:2622–2622.
  47. Rader EP, Turk R, Willer T, Beltrán D, Inamori K, Peterson TA, Engle J, Prouty S, Matsumura K, Saito F, Anderson ME, Campbell KP: Role of dystroglycan in limiting contraction-induced injury to the sarcomeric cytoskeleton of mature skeletal muscle. *Proc Natl Acad Sci* 2016, 113:10992–10997.
  48. Xie X, Tsai SY, Tsai MJ: COUP-TFII regulates satellite cell function and muscular dystrophy. *J Clin*

- Invest 2016, 126:3929–3941.
49. Alexakis C, Partridge T, Bou-Gharios G: Implication of the satellite cell in dystrophic muscle fibrosis: a self-perpetuating mechanism of collagen overproduction. *AJP Cell Physiol* 2007, 293:661–669.
  50. Young CNJ, Chira N, Róg J, Al-Khalidi R, Benard M, Galas L, Chan P, Vaudry D, Zabłocki K, Górecki DC: Sustained activation of P2X7 induces MMP-2-evoked cleavage and functional purinoceptor inhibition. *J Mol Cell Biol* 2017, 10:229–242.
  51. Merrick D, Stadler LKJ, Larner D, Smith J: Muscular dystrophy begins early in embryonic development deriving from stem cell loss and disrupted skeletal muscle formation. *Dis Model Mech* 2009, 2:374–388.
  52. Howard PL, Dally GY, Ditta SD, Austin RC, Worton RG, Klamut HJ, Ray PN: Dystrophin isoforms Dp71 and Dp427 have distinct roles in myogenic cells. *Muscle and Nerve* 1999, 22:16–27.
  53. Sarig R, Mezger-Lallemand V, Gitelman I, Davis C, Fuchs O, Yaffe D, Nudel U: Targeted inactivation of Dp71, the major non-muscle product of the DMD gene: Differential activity of the Dp71 promoter during development. *Hum Mol Genet* 1999, 8:1–10.
  54. Kudoh H, Ikeda H, Kakitani M, Ueda A, Hayasaka M, Tomizuka K, Hanaoka K: A new model mouse for Duchenne muscular dystrophy produced by 2.4 Mb deletion of dystrophin gene using Cre-loxP recombination system. *Biochem Biophys Res Commun* 2005, 328:507–516.
  55. Geisinger HD, Prasada Rao PVV, McDonald-Taylor CK: “mdx” Mouse myopathy: Histopathological, morphometric and histochemical observations on young mice. *J Comp Pathol* 1990, 102:249–263.
  56. Li D, Long C, Yue Y, Duan D: Sub-physiological sarcoglycan expression contributes to compensatory muscle protection in mdx mice. *Hum Mol Genet* 2009, 18:1209–1220.
  57. Pigozzo SR, Da Re L, Romualdi C, Mazzara PG, Galletta E, Fletcher S, Wilton SD, Vitiello L: Revertant Fibers in the mdx Murine Model of Duchenne Muscular Dystrophy: An Age- and Muscle-Related Reappraisal. *PLoS One* 2013, 8:1–6.
  58. Godfrey C, Muses S, McClorey G, Wells KE, Coursindel T, Terry RL, Betts C, Hammond S, O’Donovan L, Hildyard J, El Andaloussi S, Gait MJ, Wood MJ, Wells DJ: How much dystrophin is enough: the physiological consequences of different levels of dystrophin in the mdx mouse. *Hum Mol Genet* 2015, 24:4225–4237.
  59. Ferrari D, Munerati M, Melchiorri L, Hanau S, Di Virgilio F, Baricordi OR: Responses to extracellular ATP of lymphoblastoid cell lines from Duchenne muscular dystrophy patients. *AmJPhysiol* 1994, 267:886–892.
  60. Chinetti-Gbaguidi G, Colin S, Staels B: Macrophage subsets in atherosclerosis. *Nat. Rev. Cardiol.* 2015, pp. 10–17.
  61. Bauer C, Le Saux O, Pomozi V, Aherrahrou R, Kriesen R, Stölting S, Liebers A, Kessler T, Schunkert H, Erdmann J, Aherrahrou Z: Etidronate prevents dystrophic cardiac calcification by inhibiting macrophage aggregation. *Sci Rep* 2018, 8.
  62. Finckh A, Mc Carthy GM, Madigan A, Van Linthoudt D, Weber M, Neto D, Rappoport G, Blumhardt S, Kyburz D, Guerne P-A: Methotrexate in chronic-recurrent calcium pyrophosphate deposition disease: no significant effect in a randomized crossover trial. *Arthritis Res Ther* 2014, 16:458.
  63. Pomozi V, Brampton C, van de Wetering K, Zoll J, Calio B, Pham K, Owens JB, Marh J, Moisyadi S, Váradi A, Martin L, Bauer C, Erdmann J, Aherrahrou Z, Le Saux O: Pyrophosphate Supplementation Prevents Chronic and Acute Calcification in ABCC6-Deficient Mice. *Am J Pathol* 2017, 187:1258–1272.
  64. Cullen SP, Kearney CJ, Clancy DM, Martin SJ: Diverse Activators of the NLRP3 Inflammasome Promote IL-1 $\beta$  Secretion by Triggering Necrosis. *Cell Rep* 2015, 11:1535–1548.
  65. Burr AR, Molkentin JD: Genetic evidence in the mouse solidifies the calcium hypothesis of myofiber death in muscular dystrophy. *Cell Death Differ.* 2015, pp. 1402–1412.
  66. Millay DP, Goonasekera SA, Sargent MA, Maillet M, Aronow BJ, Molkentin JD: Calcium influx is sufficient to induce muscular dystrophy through a TRPC-dependent mechanism. *Proc Natl Acad Sci* 2009, 106:19023–19028.
  67. Hawellek T, Hubert J, Hischke S, Vettorazzi E, Wegscheider K, Bertrand J, Pap T, Krause M, Püschel K, Rütther W, Niemeier A: Articular cartilage calcification of the humeral head is highly prevalent and associated with osteoarthritis in the general population. *J Orthop Res* 2016, 34:1984–1990.

68. Przybyl J, Kowalewska M, Quattrone A, Dewaele B, Vanspauwen V, Varma S, Vennam S, Newman AM, Swierniak M, Bakula-Zalewska E, Siedlecki JA, Bidzinski M, Cools J, van de Rijn M, Debiec-Rychter M: Macrophage infiltration and genetic landscape of undifferentiated uterine sarcomas. *JCI Insight*, American Society for Clinical Investigation, 2017, 2:e94033.
69. Jablonski KL, Chonchol M: Vascular calcification in end-stage renal disease. *Hemodial Int* 2013, 17 Suppl 1:S17-21.
70. Regard JB, Malhotra D, Gvozdenovic-Jeremic J, Josey M, Chen M, Weinstein LS, Lu J, Shore EM, Kaplan FS, Yang Y: Activation of hedgehog signaling by loss of GNAS causes heterotopic ossification. *Nat Med* 2013, 19:1505–1512.
71. King JB: Post-traumatic ectopic calcification in the muscles of athletes: A review. *Br J Sports Med* 1998, 32:287–290.
72. Dalloz C, Sarig R, Fort P, Yaffe D, Bordais A, Pannicke T, Grosche J, Mornet D, Reichenbach A, Sahel J, Nudel U, Rendon A: Targeted inactivation of dystrophin gene product Dp71: Phenotypic impact in mouse retina. *Hum. Mol. Genet.* 2003, pp. 1543–1554.
73. Fort PE, Darche M, Sahel JA, Rendon A, Tadayoni R: Lack of dystrophin protein Dp71 results in progressive cataract formation due to loss of fiber cell organization. *Mol Vis* 2014, 4:1480–1490
74. Takatoh J, Kudoh H, Kondo S, Hanaoka K. Loss of short dystrophin isoform Dp71 in olfactory ensheathing cells causes vomeronasal nerve defasciculation in mouse olfactory system. *Exp Neurol.* 2008 Sep;213(1):36-47.
75. Cox GA, Sunada Y, Campbell KP, Chamberlain JS: Dp71 can restore the dystrophin-associated glycoprotein complex in muscle but fails to prevent dystrophy. *Nat Genet* 1994, 8:333–339.
76. Greenberg DS, Sunada Y, Campbell KP, Yaffe D, Nudel U: Exogenous Dp71 restores the levels of dystrophin associated proteins but does not alleviate muscle damage in mdx mice. *Nat Genet* 1994, 8:340–344.

## FIGURE LEGENDS

**Figure 1: Dystrophin isoform expression in *mdx* vs *mdx*<sup>*βgeo*</sup> muscle.** (A) DMD mutation location and their effects on predicted isoform expression in *mdx* and *mdx*<sup>*βgeo*</sup>. The *mdx* mouse carries a point mutation in exon 23, whereas *mdx*<sup>*βgeo*</sup> harbours an insertion disrupting the reading frame downstream from exon 63. Isoforms predicted to be expressed or not are shown in green or red, respectively. (B) Western blot analysis of dystrophin protein expression in 8 week muscles showing loss of the Dp427 isoform in *mdx* samples and loss of all isoforms from *mdx*<sup>*βgeo*</sup>, which confirmed it to be a complete dystrophin KO. Triplicate bands shown represent lysates from three different animals and actin is shown as a protein loading control.

**Figure 2: Morphological and functional alteration in *mdx* vs *mdx*<sup>*βgeo*</sup> muscle.** Morphometric analysis of 8 week TA muscles revealed a significant shift in (A) fibre size in the order of: Wt > *mdx* > *mdx*<sup>*βgeo*</sup>, which was found to be consistent for the average fibre area (B) and ferret diameter (C). Insets in A depict example of fibre thresholding and the analysis using ImageJ. Numbers of centrally nucleated fibres were significantly elevated: *mdx*<sup>*βgeo*</sup> > *mdx* > Wt (D). Serum CK levels indicative of sarcolemma stability were not significantly altered in *mdx*<sup>*βgeo*</sup> compared to *mdx* (E). Grip strength at 8 weeks was reduced by around 50% in both *mdx* and *mdx*<sup>*βgeo*</sup> compared to Wt (F) and diaphragm contractile force was also low in both *mdx* and *mdx*<sup>*βgeo*</sup>. In contrast, at 12 months, increases in maximum force were recorded in both Wt and *mdx*, but not in *mdx*<sup>*βgeo*</sup> diaphragms, which remained at a basal level (G). Picro Sirius Red staining for collagen (H) and Oil Red O staining for fat



(I) in 8 week vs. 12 month diaphragms revealed significant increases in older animals:  $mdx^{\beta geo} > mdx > Wt$ . Data are presented as the mean  $\pm$  SD,  $n = 3-5$ , \* $P < 0.05$ , \*\*\* $P < 0.001$ , \*\*\*\* $P < 0.0001$ . Scale bars (shown in H and I): 250  $\mu m$ .

**Figure 3: Muscle fibre mineralisations linked to loss of dystrophin expression in  $mdx$  and  $mdx^{\beta geo}$ .** Immunohistochemistry staining for dystrophin in 8 week TA muscle sections (A) confirmed the  $mdx$  to express dystrophin in a small number of revertant fibres. In contrast,  $mdx^{\beta geo}$  animals displayed no revertant fibres, in keeping with the molecular alteration in these animals. (B) Upon dissection, significant white striations (red arrows) were observed in the diaphragms of  $mdx^{\beta geo}$ , which were also found in  $mdx$  albeit at much lower levels but not in controls. Heightened diaphragm hypercontraction was also consistently observed in the order of:  $mdx^{\beta geo} > mdx > Wt$ , represented by the enlarged region of translucent connective tissue in the centre. Striations were found in all skeletal muscle groups of dystrophic mice but at different levels, with proximal muscles (quadriceps and gluteus) being affected more than distal muscles such as TA (C). Heart muscles were also found to be affected, albeit showing slightly different striation patterns than skeletal muscles (D & Supplementary Figure 1). Scale bar (shown in A): 100 $\mu m$ .

**Figure 4: Histochemical and mineral analyses in 8-week-old  $mdx$  and  $mdx^{\beta geo}$  muscles.**

Alizarin red (A) and Von Kossa staining (B) demonstrated that the white striations in diaphragm sections contained calcium and phosphate, respectively. (C) Electron backscatter diffraction (EBSD) analysis of diaphragm sections from 8 week  $mdx^{\beta geo}$  identified co-localisation of calcium (D) and phosphate (E) in electron-dense fibres, with the Ca:P ratio of 1.50 (4F), consistent with the presence of Tricalcium Phosphate [ $Ca_3(PO_4)_2$ ] or hydroxyapatite, which has a ratio of 1.6729;  $n = 3$  mice. Scale bar = 250  $\mu m$ .

**Figure 5: Whole body and 3D muscle analysis of ectopic calcifications in  $mdx$  and  $mdx^{\beta geo}$ .**

Whole-body tissue clearing and AR staining show distribution of ectopic calcification across the entire musculature. Representative bright-field and epifluorescent images (A, upper and lower, respectively) reveal sites of myofibre calcification and allow detailed comparative imaging of the affected body regions. (B) Epifluorescent images of the selected planes from A demonstrate higher prevalence of calcifications in  $mdx^{\beta geo}$  vs.  $mdx$  with a complete absence of deposits in the control mouse. Arrowheads indicate clusters of calcium deposits in laryngopharynx (1-3), forelimb (4-6), diaphragm (7-9), lumbar region (10-12) and hind limb (13-15). *Spinalis pars lumborum* from macroscopically pre-screened mice were isolated and imaged in crossed polarized light (C) and light-sheet fluorescence microscopy (D), scale bar = 5mm. 3-dimensional light-sheet data allows to reconstruct distribution of sites of ectopic calcification (E) and quantify its pattern in muscles of  $mdx^{\beta geo}$  and  $mdx$  - presented here as % mineralization and cumulative frequency distributions in triceps brachii, spinalis pars lumborum and biceps femoris (F). Unpaired t-test; two-sample Kolmogorov-Smirnov test, \* $P < 0.05$ , \*\* $P < 0.01$ ,  $n = 3$  mice per group, mean  $\pm$  SD.

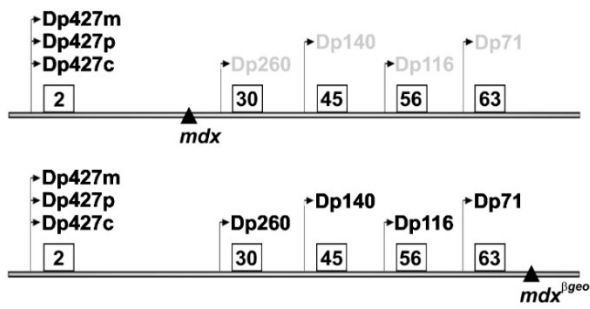
**Figure 6: Quantification of muscle fibre mineralisations in *mdx* vs *mdx* <sup>$\beta$ geo</sup>.** Alizarin Red staining was quantified in *mdx* (A) and *mdx* <sup>$\beta$ geo</sup> (B) diaphragms at 8 weeks of age. Representative images of TA sections from *mdx* (C) and *mdx* <sup>$\beta$ geo</sup> (D) are shown to illustrate the difference in severity between different muscle groups. Alizarin Red images were thresholded, a mask was generated in ImageJ (E) and fibres displaying an arbitrarily assigned positive value at or above the threshold level were counted using the ImageJ particle analysis function. (F) A significant increase in absolute numbers and % of mineralized muscle fibres was found in *mdx* <sup>$\beta$ geo</sup> compared to age-matched *mdx* diaphragms. Striations along the entire length of fibres were analyzed in whole muscle mineralization analysis using 3D X-ray imaging (G-J), scale bar = 5 mm. Quadriceps from 8-week-old *mdx* (G) and *mdx* <sup>$\beta$ geo</sup> (H) in 3D rendering revealed two different patterns of mineralization; one diffuse and globular and the other striated (left and right side of tissue shown in H, respectively). Representative Z- sections for *mdx* and *mdx* <sup>$\beta$ geo</sup> are shown in (I) and (J), respectively. Data are presented as the mean  $\pm$  SD, n=3, \*\*\*\*P < 0.0001.

**Figure 7: Timing and evolution of muscle fibre mineralization in *mdx* <sup>$\beta$ geo</sup> muscles.** At 2 weeks, muscles appear normal with no visible striations (A-C). By 4 weeks (D-F), light striations begin to appear (arrowed). Following a peak at around 2 months (G), calcium containing fibres (arrowed) disappear at around 10-12 weeks (H), and are replaced by connective tissue (I). Note the increased opacity of the diaphragm with increasing age (G to I progression). (J) Quantification of AR-positive fibres across ages and (K) Quantification of AR staining in 2, 3 and 6 month old diaphragm sections confirming the absence of mineralization. Data are presented as the mean  $\pm$  SD, n=3, \*\*\*\*P < 0.0001.

**Figure 8: Differential macrophages distribution and association with mineralized fibres in *mdx* and *mdx* <sup>$\beta$ geo</sup> muscles.** (A) Confocal image showing F4/80 (red) macrophage marker and cell nuclei (blue) staining combined with mineral deposits visualized in bright-field in *mdx* <sup>$\beta$ geo</sup> diaphragms. Calcified fibres can be seen saturated with macrophages (B, arrowed). Macrophage distribution differs between *mdx* and *mdx* <sup>$\beta$ geo</sup> muscles: In *mdx* diaphragm (C), macrophages can be seen distributed throughout the tissue with some areas of increased infiltration while in *mdx* <sup>$\beta$ geo</sup> macrophages appear to be predominantly associated with calcified fibres (D). (E-H) Confocal images of F4/80 staining without brightfield corresponding with (A-D). Higher magnification images (I-K) showing CD68 (red) marker co-localisation with osteopontin (green) indicating the predominantly M1 phenotype of macrophages associated with calcified fibres. (L) ImageJ-based quantification of images showing the CD68 staining to localize to fewer (left panel) but larger (middle) ‘puncta’ in *mdx* <sup>$\beta$ geo</sup>, confirming macrophage clustering at sites of mineralization. Significant differences in CD68 puncta number and size were found between *mdx* and *mdx* <sup>$\beta$ geo</sup> (M, left and centre), but total CD68 intensity in *mdx* <sup>$\beta$ geo</sup> was not found significantly different to that of *mdx* (M, right). Data are presented as the mean  $\pm$  SD, n=3, \*\*\*\*P < 0.0001. Scale bars (shown in A, C & D): 250  $\mu$ m, (shown in B): 50  $\mu$ m, (shown in I): 100  $\mu$ m.

# Figures

**A**



**B**

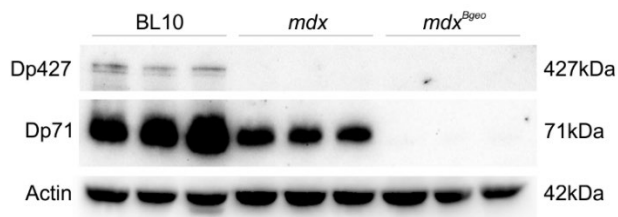


**Figure 1**

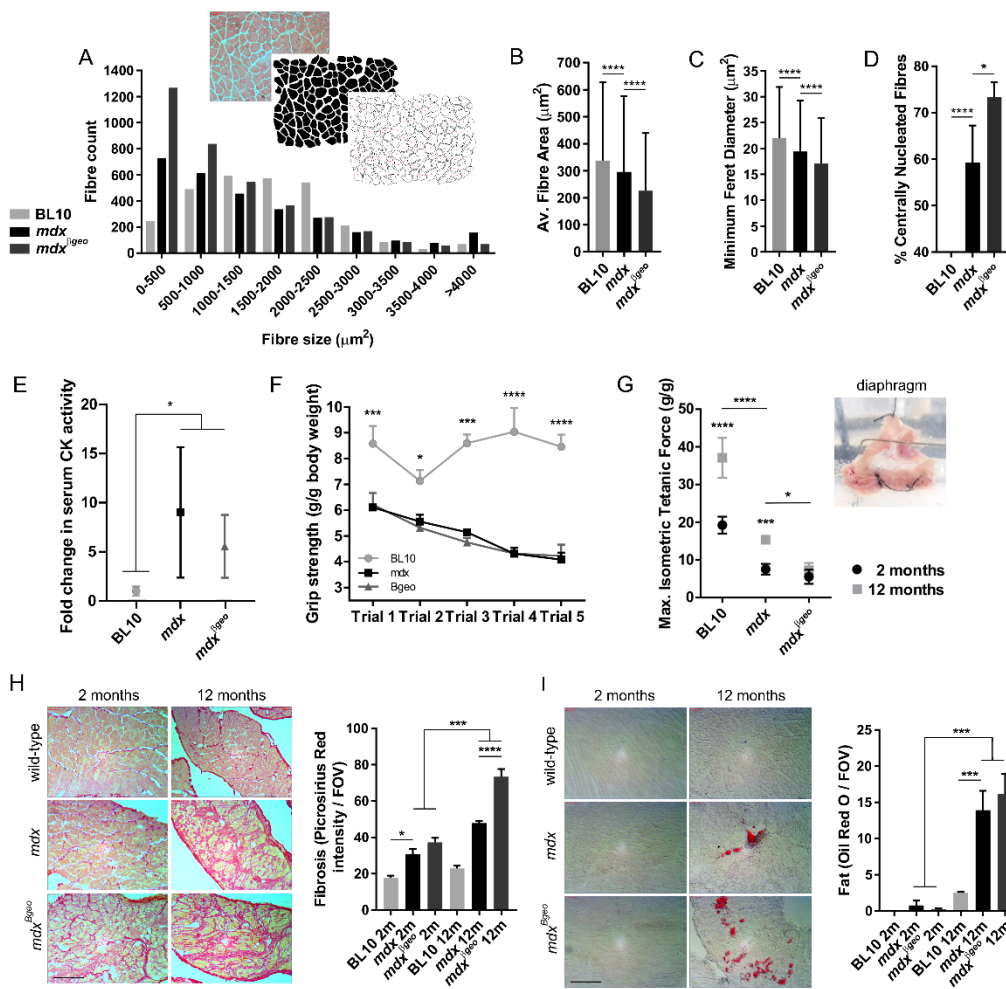


**Figure 2**

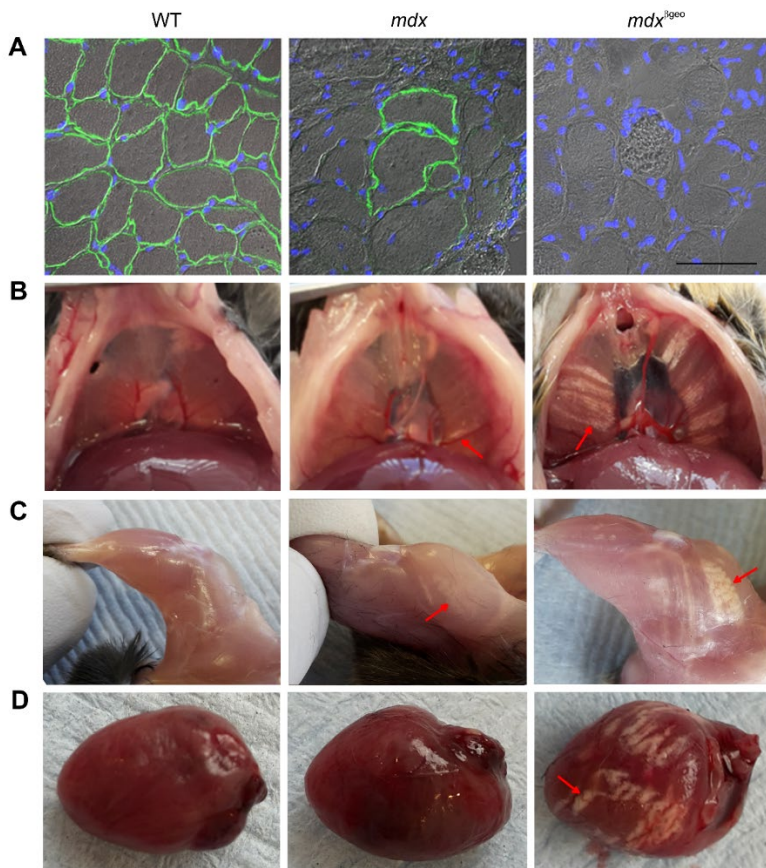


Figure 3

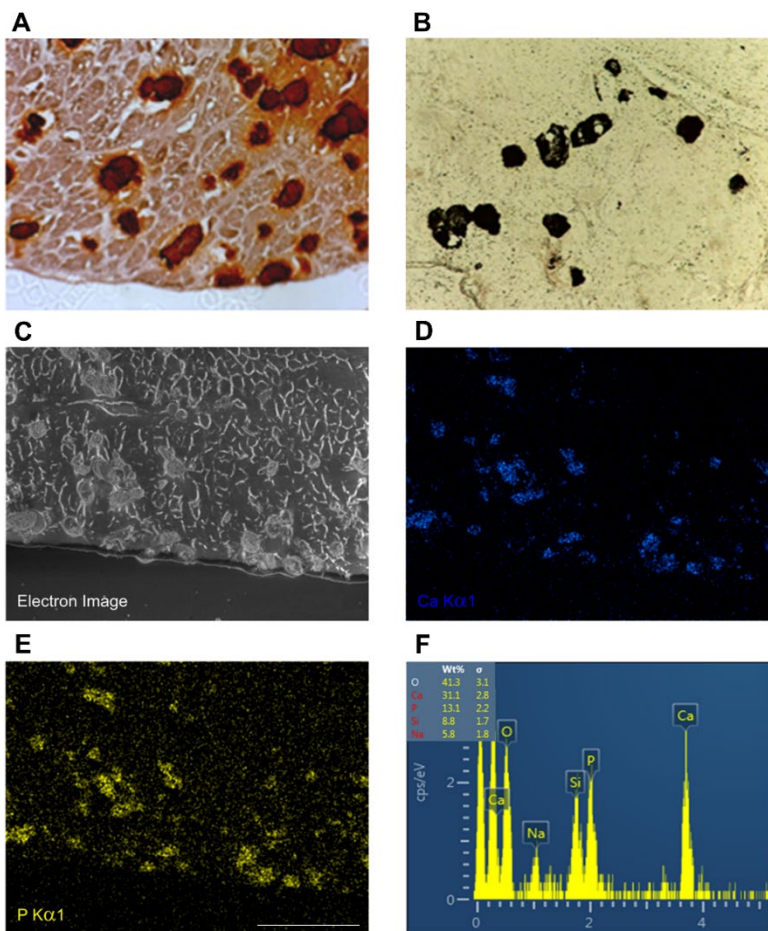


Figure 4

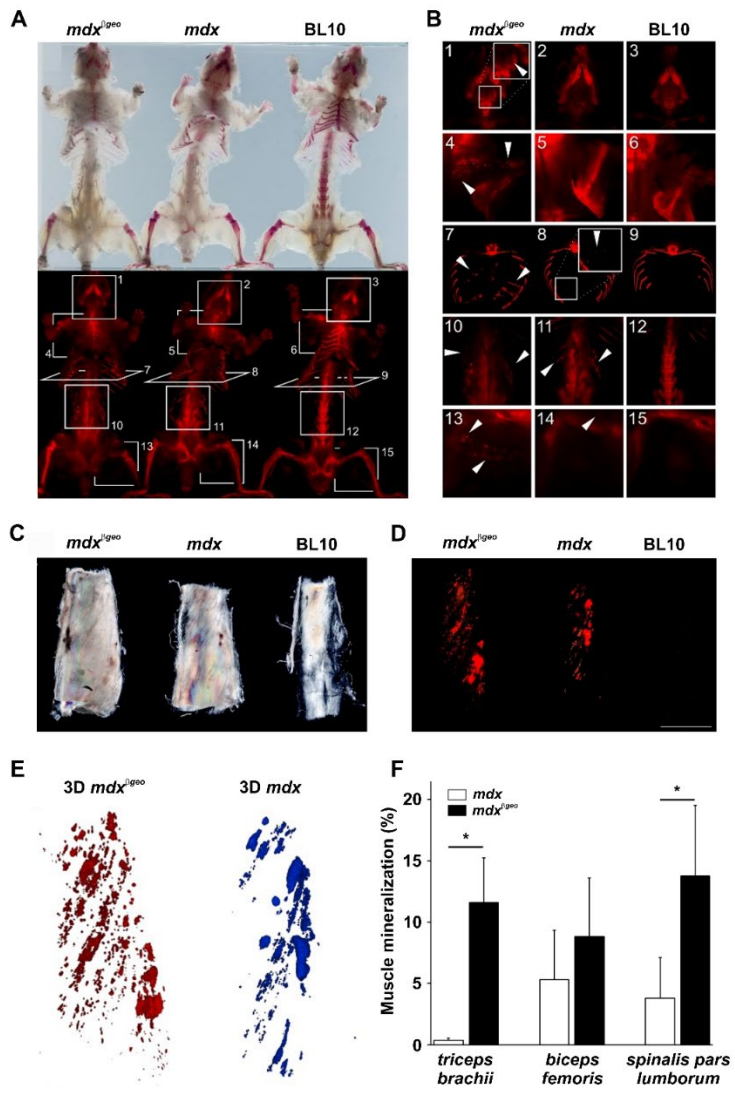
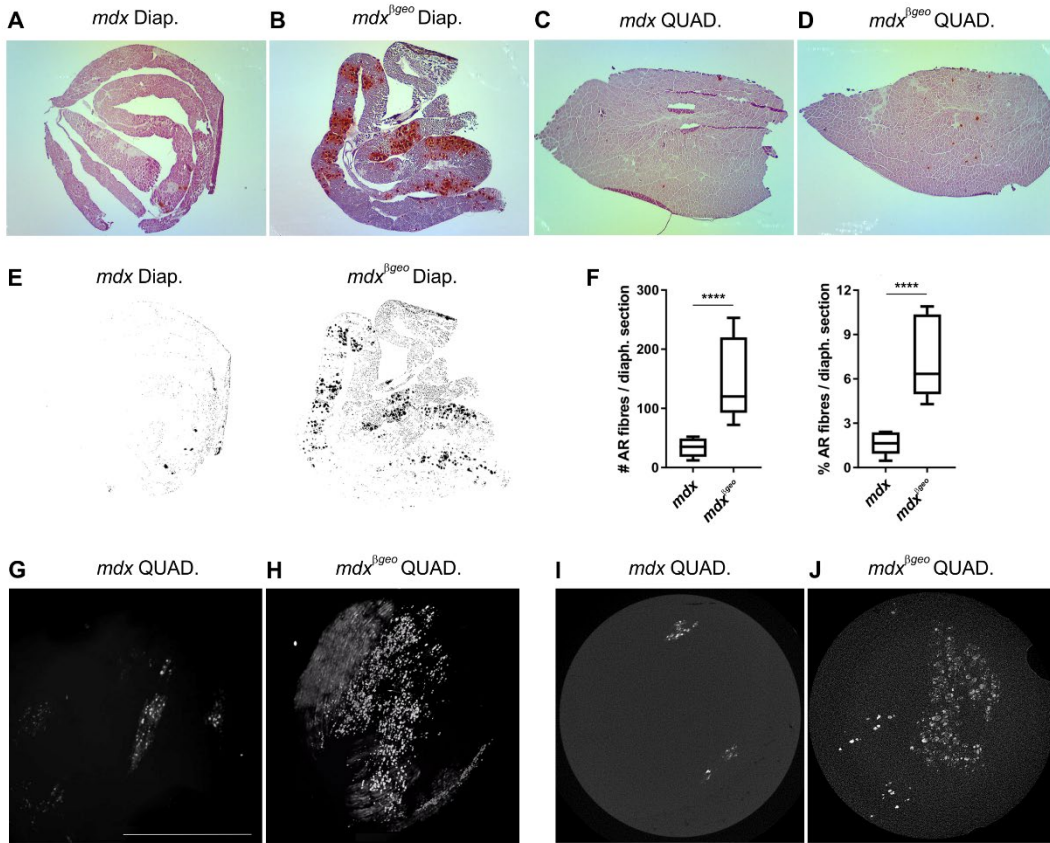


Figure 5



**Figure 6**

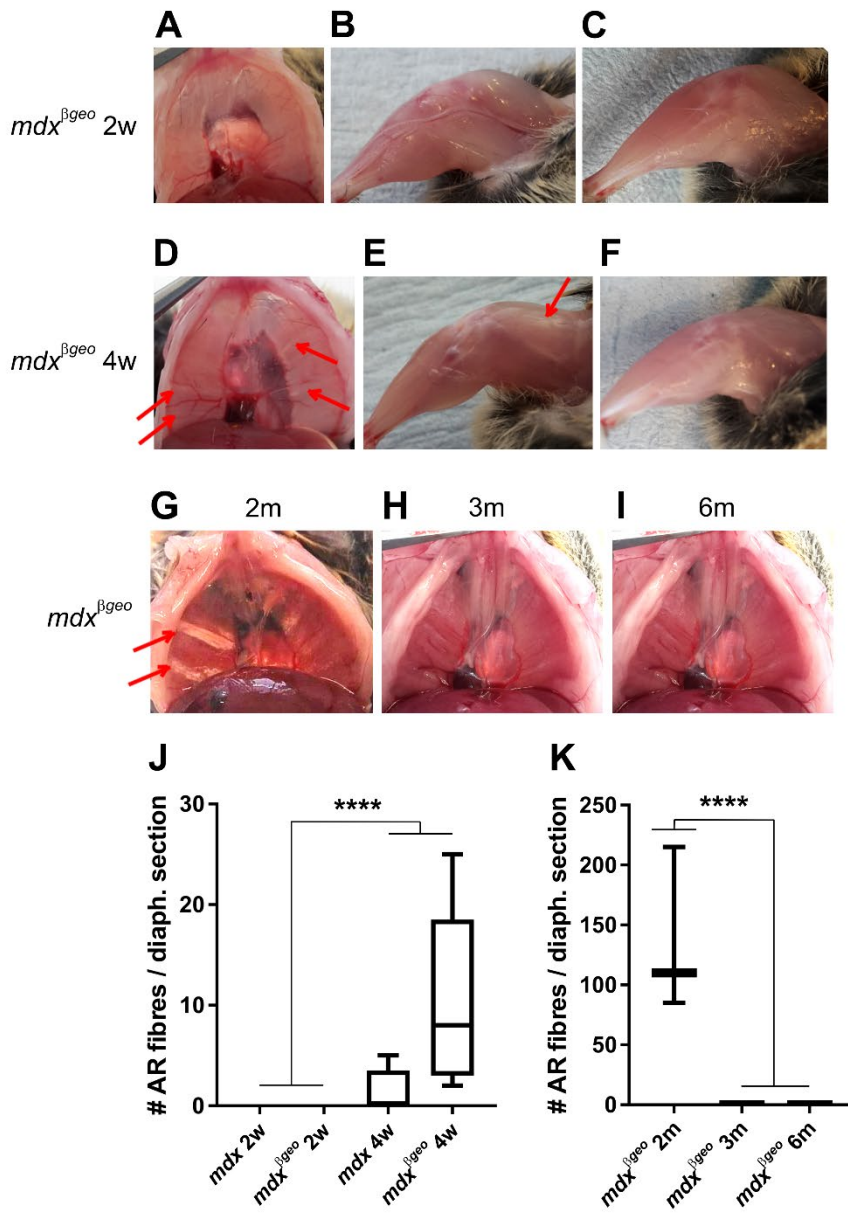


Figure 7

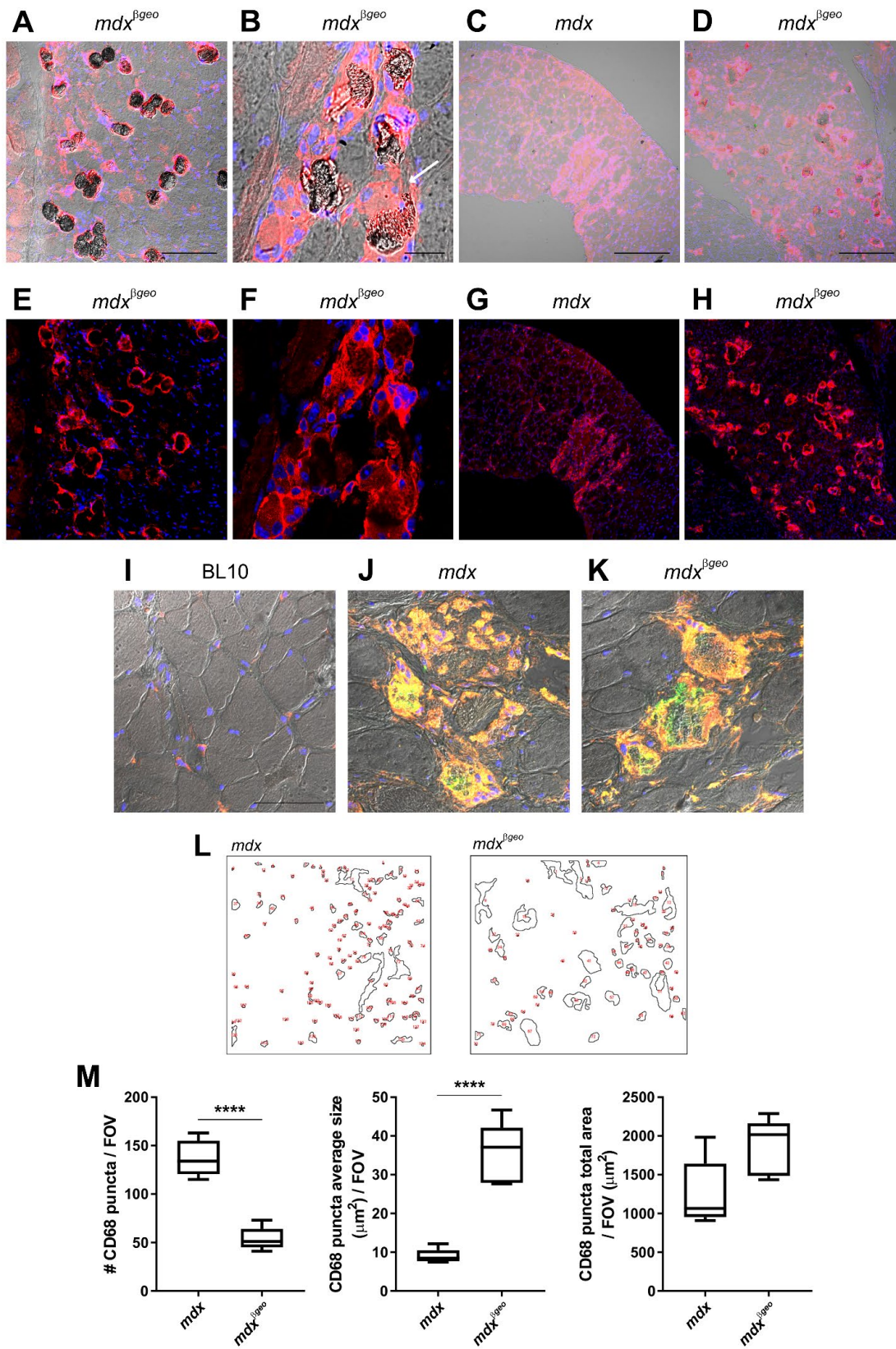


Figure 8